Research Square

Preprints are preliminary reports that have not undergone peer review.
They should not be considered conclusive, used to inform clinical practice,
or referenced by the media as validated information.

An Analytical Model for Cylindrical Rolling Resistance under Low-Speed and Heavy-Load Conditions via the Prism Contact Dynamics Limit

Zhenning Liu
Tsinghua University
Tengfei Shi
Southwest Jiaotong University
Zhen Zhao
Beihang University
Shaoze Yan
yansz@mail.tsinghua.edu.cn

Tsinghua University

Research Article

Keywords: Rolling resistance, Rolling contact, Prism contact dynamics, Contact-stress asymmetry, Energy dissipation, Hertzian switching state

Posted Date: November 13th, 2026

DOI: https://doi.org/10.21203/rs.3.rs-11398957/v1

License: This work is licensed under a Creative Commons Attribution 4.0 International License.
Read Full License

Additional Declarations: No competing interests reported.

An Analytical Model for Cylindrical Rolling Resistance under Low-Speed and Heavy-Load Conditions via the Prism Contact Dynamics Limit

Zhenning Liu[1], Tengfei Shi[2], Zhen Zhao[3], Shaoze Yan[1*]

[1]State Key Laboratory of Tribology in Advanced Equipment, Tsinghua University, Haidian, Beijing, 100084, Beijing, China.
[2]School of Mechanics and Aerospace Engineering, Southwest Jiaotong University, Chengdu, 610031, Sichuan, China.
[3]School of Aeronautic Science and Engineering, Beihang University, Haidian, Beijing, 100191, Beijing, China.

*Corresponding author(s). E-mail(s): yansz@mail.tsinghua.edu.cn;
Contributing authors: liuzn23@mails.tsinghua.edu.cn;
bhzhaozhen@buaae.edu.cn;

Abstract

Understanding the mechanism of rolling resistance is crucial for energy-efficient engineering optimization. However, precise theoretical prediction remains challenging due to the asymmetric, nonlinear, and non-smooth nature of the local contact behavior. In this paper, an analytical model of rolling resistance is established for a cylinder under low-speed and heavy-load conditions. The core idea of the proposed model is to obtain the rolling energy dissipation model of a cylinder by assuming a large side number in a polygonal rolling model. To this end, a dynamic model for a prism is first developed. Numerical simulations reveal that under low-speed and heavy-load conditions, the stress ratio between the leading and trailing edges remains approximately constant. Based on this observation, an analytical relation between the pre- and post-transition angular velocities is derived. The corresponding model for a smooth cylinder is then obtained by relating the prism edge length to the Hertzian line-contact width. This rolling resistance model is evaluated using 22 low-speed rolling experiments for Teflon, PMMA, and steel wheels, and indicates that the identified trailing-to-leading stress ratio is concentrated around 0.6 and that the velocity-dependent contribution remains small over the examined conditions. While comparison with Greenwood's classical hysteretic formulation, this model also recovers the same

characteristic dependence on normal load, contact width, and rolling radius. These results establish a direct analytical connection between repeated local contact dynamics and macroscopic rolling resistance within the low-speed and heavy-load regime.

Keywords: Rolling resistance; Rolling contact; Prism contact dynamics; Contact-stress asymmetry; Energy dissipation; Hertzian switching state

1 Introduction

Rolling resistance is a fundamental source of mechanical-energy dissipation in wheels, cylinders, disks, and other systems involving nominal rolling contact [1–7]. In the ideal rigid-body description of pure rolling, the instantaneous contact point has zero relative velocity and the normal contact force performs no work [8]. Such an idealization cannot explain the finite resistance observed in practical rolling systems. In reality, contact occurs over a finite region in which deformation and redistribution of the contact stress shift the resultant reaction away from the geometric center of the rolling body and generate a resisting moment. Understanding how this local contact process gives rise to a macroscopic rolling resistance is therefore a long-standing problem in contact mechanics and tribology.

Classical investigations have primarily attributed rolling resistance to deformation and energy dissipation within the contact region. Early work by Reynolds linked rolling resistance to the deformation of the contacting bodies, whereas Tabor and later studies distinguished the respective contributions of elastic and plastic deformation in rolling contacts [9]. Hertzian contact theory establishes the fundamental relationships among normal load, elastic properties, rolling radius, and contact size, and has thus served as the cornerstone for many analytical models of rolling resistance [10, 11]. Greenwood, Minshall, and Tabor further advanced the hysteretic interpretation, according to which a portion of the elastic energy imparted during loading is not fully recovered upon unloading [12, 13]. Other researchers have proposed that rolling resistance arises from an asymmetric pressure distribution and the consequent shift of the normal reaction away from the centre of the contact region [14, 15].

Subsequent studies have revealed that rolling resistance arises from multiple interacting mechanisms, the relative importance of which depends heavily on material properties, surface condition, geometry, load, and rolling velocity. In viscoelastic materials, hysteretic losses due to cyclic deformation are often dominant [16–20]. The associated energy dissipation is governed by the viscoelastic excitation frequency and temperature, while the effective excitation frequency itself is determined by the rolling velocity and characteristic contact length scales [21–26]. For harder materials, additional dissipative contributions arise from plastic deformation, micro-slip, adhesion, surface roughness, and repeated asperity interactions [27–38]. When the rolling contact becomes sufficiently dynamic, the contact process can also excite structural vibrations and elastic-wave propagation in the rolling body or substrate, providing additional channels for energy redistribution and dissipation [39–42]. Collectively, these findings

suggest that no single material-independent constitutive law can adequately describe rolling resistance across all operating conditions; nevertheless, the finite contact width and the asymmetry of the resulting contact reaction remain common mechanical features in many theoretical descriptions.

Studies on the mechanisms of rolling resistance also exist across a wide range of engineering rolling-contact systems, and various factors have been incorporated into the modelling of rolling resistance in these contexts. For example, in tyre–road interaction, the viscoelastic response and deformation of the tread and carcass are accounted for, leading to a dependence of rolling resistance on operating and contact conditions such as inflation pressure, road-surface texture, contact-patch characteristics, and local slip [43–49]. Wheel–rail studies have similarly demonstrated dependencies on normal load, wheel radius, material properties, traction or braking state, contact curvature, and coupled vehicle–track dynamics [50–56]. Rolling bearings and other machine elements introduce further effects associated with lubrication, conformity, surface finish, and local elastic or plastic deformation [57–60]. Although detailed models developed for these systems can predict rolling losses with considerable accuracy, their complexity is often highly specific to the corresponding application.

A parallel line of research on rolling resistance has focused on how the local rolling-contact process can be represented in analytical and numerical models. Continuum contact formulations directly resolve the pressure and deformation fields, whereas finite-element, boundary-element, and discrete-element approaches can incorporate increasingly complex material behavior and surface geometry [61–68]. Reduced-order models, by contrast, aim to retain only the dominant contact variables, such as an effective contact width, the location of the resultant reaction, or an equivalent resisting moment [69–72]. Energy-based approaches offer another useful reduction by relating the energy dissipated over one loading cycle or rolling distance to an equivalent rolling-resistance force or moment [73–79]. These methods provide efficient system-level descriptions, although the link between transient contact-force evolution and the resulting macroscopic resistance is not always explicit.

Although rolling energy losses involve multiple mechanisms, the local contact process is characterized by spatially distributed deformation and the temporal evolution of the contact boundary. Under steady rolling, these features can be represented approximately by a polygonal prism whose side length characterizes the finite contact width of an elastic cylinder. The evolution of the contact region is then represented by successive rotations about supporting corners, separated by rapid edge-to-edge contact transitions. Such transitions involve line impacts, which have been studied in non-smooth dynamics, rocking, and impact mechanics [80–84]. During each transition, the distributed contact reaction changes the translational and rotational velocities, allowing the associated mechanical-energy loss to be evaluated and related to an equivalent rolling resistance. Previous studies have also shown that the extent of the load-bearing region and the local stress distribution depend on the rolling state [85–87]. The prism therefore provides a discrete framework for connecting local contact evolution and repeated energy losses to the macroscopic rolling resistance of a cylindrical body.

Building on this discrete contact representation, our previous work developed an analytical rolling-resistance model for the high-speed, light-load regime by combining

a large-edge-number approximation of prism dynamics with an equivalent contact geometry determined by local deformation [86]. The resulting resistance moment is proportional to the square of the rolling angular velocity, providing a contact-dynamics interpretation of the velocity-dependent contribution to rolling resistance. Related experimental and theoretical investigations have examined the evolution of precession and energy dissipation during the final stages of Euler's disk motion, including the roles of rolling and sliding under different contact conditions [88–90]. Complementary modeling studies have incorporated resistance to sliding, pivoting, and rolling into non-smooth disk dynamics [91], while recent experiments and simulations have further examined the influence of substrate material properties using Coulomb and contour friction models [92]. In particular, Ma et al. showed that a phenomenological resistance torque proportional to the square of the precession rate can reproduce the measured disk dynamics under their experimental conditions [93].

However, the quadratic velocity-dependent term alone becomes vanishingly small as the rolling speed decreases and therefore cannot account for the high-load resistance observed in slowly rolling elastic wheels [94]. Extending the prism-based framework to this regime consequently requires an explicit treatment of how the sustained normal load and contact-stress asymmetry influence each contact transition. The unresolved issue is how these effects enter the angular-velocity transformation and generate a load-dependent resistance contribution through the accumulated energy loss of successive transitions.

The present study addresses this issue by developing an analytical rolling-resistance model for cylindrical bodies under low-speed and heavy-load conditions. Numerical analysis of prism contact dynamics first supports a reduced description based on full contact and an approximately constant trailing-to-leading stress ratio during each transition. Within this description, the external normal-load impulse is explicitly retained in the angular-velocity transformation, allowing the influence of the sustained load and contact-stress asymmetry on the transition-induced energy loss to be quantified. A work-equivalence relation then converts this energy loss into a continuous rolling-resistance moment, yielding distinct load-dependent and velocity-dependent contributions. Relating the prism edge length to the Hertzian line-contact width further connects these contributions to the cylinder geometry, normal load, and effective elastic modulus [10]. The formulation is evaluated through parameter identification using the low-speed rolling experiments of Kumar et al. [94] and through comparison with Greenwood's classical hysteretic model [12].

The principal contribution of this paper is an explicit analytical connection between load-affected local contact transitions and macroscopic rolling resistance, extending the prism-based framework to the high-load regime. With an appropriately identified stress-asymmetry parameter, the resulting expressions can support rolling-resistance and driving-force estimates, assessment of load, radius, and stiffness effects, and efficient incorporation of contact losses into system-level models of slowly rolling cylindrical components, provided that the full-contact, small-contact-width, and near-pure-rolling assumptions remain applicable.

The remainder of this paper is structured as follows. Section 2 formulates the rolling and line-contact dynamics of the prism and examines the relevant contact

characteristics; Section 3 derives the analytical rolling-resistance model and introduces the Hertzian contact-width mapping; Section 4 presents the model evaluation and comparison; and Section 5 summarizes the principal conclusions and range of applicability.

2 Dynamic analysis of a rolling prism

This section investigates the dynamics of a prism rolling on a plane. When the number of polygon edges is sufficiently large, the rolling motion is observed to alternate between two distinct processes: rotation about successive vertices and edge-to-edge contact. The dynamical characteristics of these processes will provide a fundamental basis for analyzing energy dissipation.

2.1 Kinematic and contact description of a rolling prism

Fig. 1 shows a regular prism with an N-sided cross-section rolling on a horizontal plane. The prism has mass m, circumradius r, axial length l, and mass moment of inertia J about its centroid C. The half central angle is $\alpha = \pi/N$, and the corresponding side length is $l_b = 2r\sin\alpha$. A horizontal driving force F_{px} and a total downward load F_{py}, including the prism weight, are applied through the centroid. A fixed coordinate system $(O; X, Y)$ is introduced, with the X-axis aligned with the supporting plane. Based on the relative position of the prism's centroid to the origin of the coordinates, as well as the angle between the prism's edges and the coordinate axes, the motion of the prism can be described by the translations x and y, along with a rotation θ.

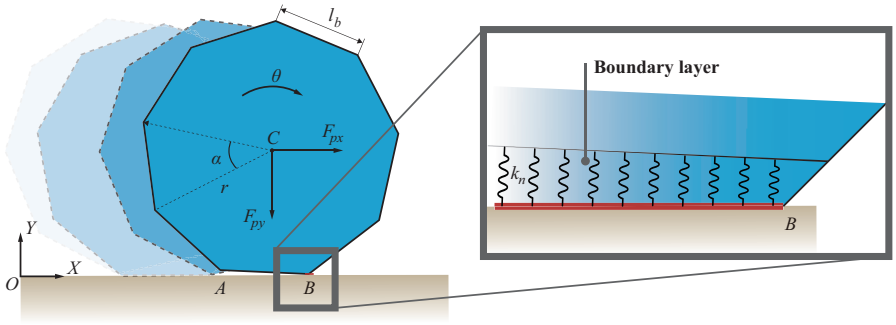


Fig. 1 Schematic of a polygonal prism rolling on a horizontal plane under a driving force F_{px} and a normal load F_{py}. Points A and B denote the trailing and leading corners of the contact face, respectively. The enlarged view illustrates the elastic boundary layer, represented by distributed normal springs with effective stiffness per unit area k_n.

As the prism rolls on the plane, its motion alternates between corner-pivot rotation and contact transition. In the first phase, the prism rotates about the supporting corner until the adjacent face comes into contact with the plane. In the second phase, a distributed contact reaction develops over this face, and the support point shifts from the trailing corner A to the leading corner B. Although the contact process is typically of short duration, the stress distribution within the contact region undergoes

a complex evolution, which cannot be captured by a quasi-static or instantaneous contact assumption.

To capture the stress evolution within the contact region, a thin, homogeneous elastic boundary layer of undeformed thickness Δ is introduced between the prism and the supporting plane. This layer models the effective normal compliance of the contacting bodies, and its deformation is bounded by the prism face and the supporting plane. On the nominal contact face, a local coordinate system $(O'; X', Y')$ is defined with its origin at the trailing corner A, with its X'-axis directed towards B and the Y'-axis normal to the face. In this coordinate, the position along the contact face can be denoted by $\xi \in [0, l_b]$.

Under the assumption of a linear elastic foundation, the normal stress is related to the local compression through

$$\sigma_n(\xi, t) = k_n \delta_n(\xi, t), \qquad k_n = \frac{E^*_{\mathrm{bl}}}{\Delta}, \tag{1}$$

where σ_n is the normal stress, $\delta_n(\xi, t) \geq 0$ is the compressive deformation of the layer, k_n is the effective normal stiffness per unit area, and E^*_{bl} is the effective normal modulus assigned to the boundary layer. For a plane-strain layer, $E^*_{\mathrm{bl}} = E/(1-\nu^2)$, where E and ν are its Young's modulus and Poisson's ratio, respectively.

The contact is unilateral: the layer transmits only compression. The local compression is defined as $\delta_n(\xi, t) \geq 0$, with $\delta_n > 0$ corresponding to an active contact and $\delta_n = 0$ to a separated state in which no normal stress is transmitted. Under the small-deformation approximation and for rigid contacting faces, δ_n varies linearly over the active contact region $\mathcal{A}(t) = \{\xi : \delta_n > 0\}$; since Δ, k_n, and E^*_{bl} are uniform, $\sigma_n(\xi, t)$ is likewise linear over $\mathcal{A}(t)$. The region $\mathcal{A}(t)$ evolves with the compression, possibly spanning only part of the nominal edge. Tangentially, a Coulomb law $|\sigma_t| \leq \mu_s \sigma_n$ is adopted, with equality for sliding and strict inequality for sticking. Here, μ_s and μ_k the coefficients of static and kinetic friction, respectively. These relations form the basis for the numerical study. For a detailed description of how to simulate the dynamics of a polygonal prism, see [86]. In the following subsection, we provide a brief introduction to the dynamics of the rolling prism.

2.2 Dynamics equations of the rolling prism

The rolling motion considered here consists of two successive stages: rotation about a supporting corner and a contact transition as the adjacent face comes into contact with the plane. During the first stage, the prism undergoes approximately rigid rotation about the supporting corner. During the second stage, a distributed contact reaction develops, and the support is transferred to the next corner.

During corner-pivot rotation, as shown in Fig.2(a), the supporting corner A is assumed to remain stationary, provided that the contact reaction satisfies the unilateral-contact and sticking conditions. The prism motion is then fully described by the rotation angle θ. Taking moments about A gives

$$(J + mr^2)\ddot{\theta} = -F_{py} r \sin(\alpha - \theta), \tag{2}$$

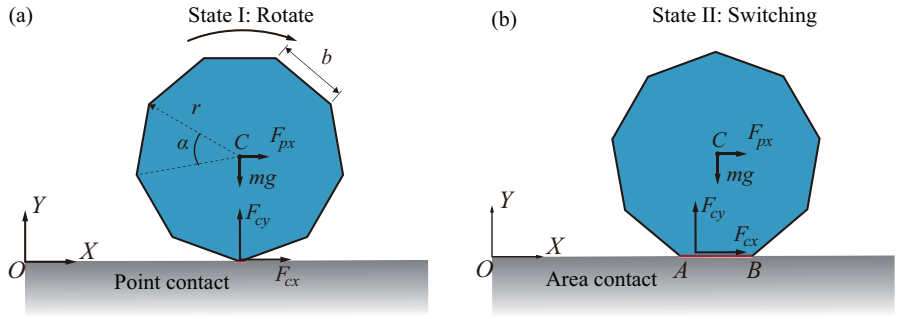


Fig. 2 Schematic view of the rolling prism. The motion alternates between (a) a slow rotation state and (b) a rapid switching state.

where m is the prism mass, J is the mass moment of inertia about its centroid, and $\alpha = \pi/N$ is the half central angle associated with one polygon edge. Since the contact reaction acts at the supporting corner, it produces no moment about the pivot. The corner-pivot stage is therefore conservative, with no dissipative contact effects. We can integrate Equation (2) to track the rotation of the prism until the adjacent face comes into contact with the supporting plane.

Once the adjacent face contacts the supporting plane, the contact becomes a line contact along this face. During this stage, the translational and rotational motions are governed by

$$\begin{cases} m\ddot{x} &= F_{px} + F_{cx}, \\ m\ddot{y} &= F_{cy} - F_{py}, \\ J\ddot{\theta} &= M_{cx} + M_{cy}, \end{cases} \tag{3}$$

where F_{cx} and F_{cy} are the tangential and normal contact resultants, respectively, and M_{cx} and M_{cy} are their moments about the centroid. All four quantities are obtained by integrating the contact stress distribution over the active contact region $\mathcal{A}(t)$.

The distributed normal reaction is evaluated using the elastic boundary layer introduced above. At each integration step, the prism configuration gives the local separation between the contact face and the plane; comparing it with the undeformed thickness Δ yields the local compression $\delta_n(\xi, t)$. The normal stress then follows from Eq. (1) wherever $\delta_n > 0$, and vanishes elsewhere. The load-bearing region $\mathcal{A}(t)$ thus evolves directly with the boundary-layer deformation. Assuming that the normal stress to be uniform along the axial length l, the normal contact resultant and its moment about the centroid are given by

$$\begin{cases} F_{cy}(t) &= l \int_0^{l_b} \sigma_n(\xi, t)\, \mathrm{d}\xi, \\ M_{cy}(t) &= l \int_0^{l_b} \big[x(\xi, t) - x(t)\big] \sigma_n(\xi, t)\, \mathrm{d}\xi, \end{cases} \tag{4}$$

where $x(\xi, t)$ is the global horizontal coordinate of the contact location identified by ξ, and $x(t)$ is the centroid coordinate. Since separated locations carry zero stress, these integrals automatically account for changes in the contact extent without prescribing a particular stress-distribution mode.

The tangential reaction is governed by a Coulomb friction law applied pointwise over the active contact region $\mathcal{A}(t)$, $|\sigma_t(\xi,t)| \le \mu_s \sigma_n(\xi,t)$, with equality corresponding to sliding. Under the sticking case, the tangential relative velocity vanishes over $\mathcal{A}(t)$, and the resultant F_{cx} is obtained implicitly from the equations of motion. Sticking is admissible only if the resulting F_{cx} satisfies $|F_{cx}| \le \mu_s F_{cy}$; otherwise, sliding occurs, with $\sigma_t(\xi,t) = -\mu_k \sigma_n(\xi,t)\,\mathrm{sgn}(\dot{\xi}_r)$ and the resultants evaluated by integration over $\mathcal{A}(t)$.

During the contact transition, Eq. (3) is integrated while updating the boundary-layer compression, contact resultants, and friction state. The transition is completed when support has transferred to corner B and the contact kinematics permit rotation about that corner. The resulting angular position and velocity, θ and $\dot{\theta}$, then serve as the initial conditions for the next corner-pivot stage, in which the motion is again governed by Eq. (2) with B as the new supporting corner. Repeating these stages yields the rolling motion and the local stress evolution during successive contact events.

2.3 Numerical analysis of the contact characteristics

Numerical simulations were performed using the boundary-layer model to investigate the contact characteristics of a rolling prism. A homogeneous regular steel prism with $N = 30$, $r = 15$ mm, and $l = 50$ mm was considered, with a rough glass surface as the supporting plane. The steel density was $\rho = 7.85 \times 10^3$ kg/m^3. The prism mass and its mass moment of inertia about the centroidal axis parallel to the prism axis were calculated of approximately 0.275 kg.

The combined normal compliance of the steel prism and the glass plane was represented by an effective boundary-layer modulus of $E^*_{\mathrm{bl}} = 5.57 \times 10^{10}$ Pa. This value incorporates the elastic compliance of both contacting bodies. The undeformed boundary-layer thickness was set to $\Delta = 2$ mm, and the corresponding normal stiffness per unit area was determined from $k_n = E^*_{\mathrm{bl}}/\Delta$. The coefficients of static and kinetic friction were set to $\mu_s = 0.12$ and $\mu_k = 0.10$, respectively.

Different horizontal driving forces were applied under a prescribed total normal load to examine the rolling response and the associated contact evolution. The loading conditions were expressed in terms of the prism weight mg, where $g = 9.81$ m/s^2 is the gravitational acceleration.

Fig. 3 presents two representative histories of the centroid velocity under a normal load of $F_{py} = 100mg$. Under the lower driving force, $F_{px} = mg$, the rolling velocity gradually approaches a quasi-steady mean value, with small periodic fluctuations arising from successive contact transitions, as shown in Fig. 3(a). Under the higher driving force, $F_{px} = 3mg$, the prism accelerates monotonically over the simulated interval and reaches substantially higher velocities, as shown in Fig. 3(b). These two cases provide representative lower- and higher-speed conditions for examining how the local contact behavior evolves during rolling.

To investigate the local contact mechanisms underlying these rolling responses, the boundary-layer deformation and the normal-stress distribution were analyzed over successive contact transitions. At the lower driving force, the compressive stress spans the entire nominal contact face, with both the trailing corner A and the leading corner B remaining in contact with the plane. At the higher driving force, the trailing region

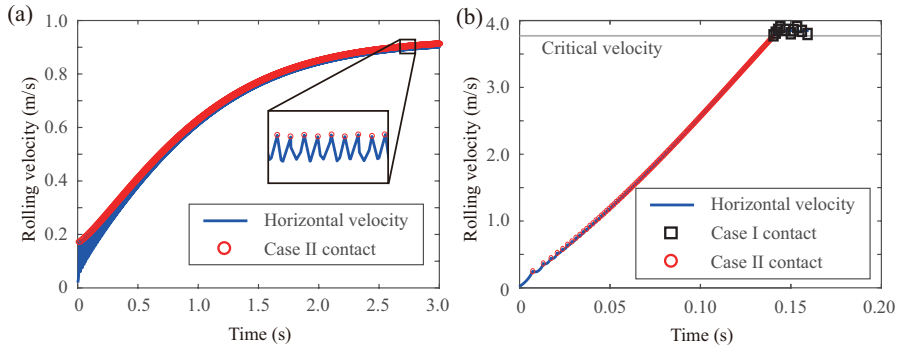


Fig. 3 Representative rolling-velocity histories under a normal load of $F_{py} = 100mg$: (a) $F_{px} = mg$; and (b) $F_{px} = 3mg$. The markers indicate the contact configurations identified from the calculated stress distributions, with Case-I and Case-II denoting partial and full contact, respectively.

reaches zero stress and separates, whereas the region toward B remains compressed. This variation in the extent and asymmetry of the stress distribution alters the normal contact resultant and its moment, and consequently the angular momentum transfer about the supporting corner during each transition.

These two representative stress distributions are shown in Fig. 4. The partial-contact configuration, denoted Case I, is one in which the normal reaction is carried by only part of the nominal contact face toward B. The full-contact configuration, denoted Case II, is one in which the compressive stress spans the entire nominal face.

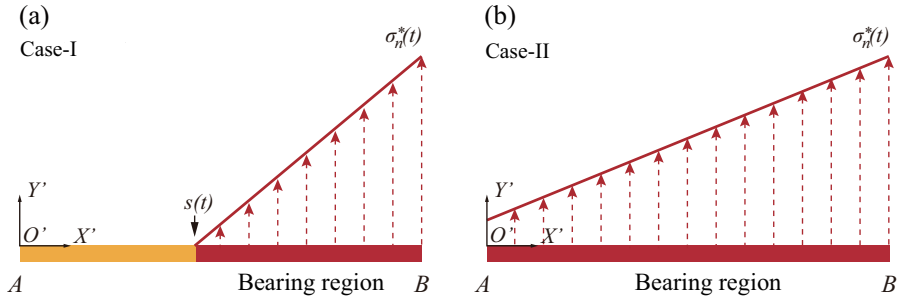


Fig. 4 Schematic illustration of the two contact configurations observed during contact transitions: (a) Case-I, with a separated trailing region and a partially compressed face; and (b) Case-II, with compressive stress distributed over the entire nominal contact face.

For the linear stress profiles illustrated in Fig. 4, let $s(t)$ denote the zero-stress position measured from corner A along the previously defined local coordinate. In Case I, $0 < s(t) < l_b$, so $s(t)$ is the actual boundary between the separated and load-bearing regions. In Case II, the stress increases toward B and remains positive at A; extrapolating the linear profile beyond A therefore gives a virtual zero-stress position $s(t) < 0$. The limiting condition $s(t) = 0$ corresponds to vanishing stress at A and marks the transition between partial and full contact.

The contact-mode markers in Fig. 3 show how the two stress configurations evolve during rolling. Under the lower driving force, the successive contact transitions remain classified as Case II throughout the simulated interval. Under the higher driving force, the transitions initially remain in Case II, but a transition to Case I occurs once the velocity exceeds a threshold value. Thus, under the prescribed normal load, the lower-speed response corresponds to sustained full contact during the transitions, whereas the higher-speed response may involve separation of the trailing region.

To further quantify the stress evolution within Case II, a trailing-to-leading stress ratio is introduced as $c(t) = \sigma_A(t)/\sigma_B(t)$, where $\sigma_A(t)$ and $\sigma_B(t)$ denote the normal stresses at corners A and B, respectively. Fig. 5 shows the evolution of $c(t)$ during representative Case II transitions at different rolling speeds. Since the transition duration varies with the rolling speed, the elapsed contact time is normalized by the total duration of each event, which allows the histories at different speeds to be compared directly.

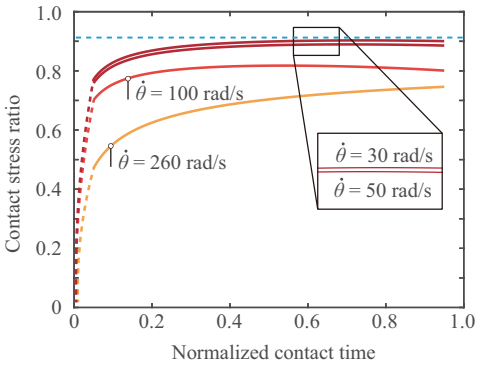


Fig. 5 Evolution of the trailing-to-leading stress ratio c during representative Case-II contact transitions at different angular velocities. The elapsed contact time is normalized by the total duration of each event.

The normalized histories reveal two distinct regimes. At relatively low rolling speeds, the stress ratio varies mainly during the initial stage of the transition and then remains nearly constant over most of the contact duration. At higher rolling speeds, the stress ratio exhibits more pronounced temporal variations. These results justify the use of an approximately constant stress ratio to represent most of an individual contact transition in the low-speed regime examined here. This ratio may nevertheless differ between operating conditions and should therefore be calibrated for each case.

The above observations motivate a reduced contact description for the low-speed, heavy-load regime considered here. In particular, full contact is assumed during each transition, and the time-dependent stress ratio is replaced by an approximately constant value. These approximations provide the basis for the derivation in the following section, where the angular-velocity transformation and the corresponding rolling-resistance expression are obtained.

3 Rolling resistance of a cylinder under low-speed and heavy-load conditions

This section develops an analytical rolling-resistance model for a cylinder, based on the reduced contact description of Section 2. Under the low-speed, heavy-load conditions considered here, each transition remains in Case II with an approximately constant stress ratio. we derive the angular-velocity transformation across a contact transition and develop an equivalent rolling-resistance model for a cylinder using a large-edge-number approximation and the Hertzian contact-width mapping.

3.1 Angular-velocity transformation across a contact transition

For the following derivation, the uniform axial length l is absorbed into the contact-stress variables, so that σ_n, σ_A, and σ_B represent axially integrated normal stresses with units of force per unit length. This convention preserves the trailing-to-leading ratio c and removes the explicit axial-length factor from the contact resultants.

Under the Case-II approximation, the entire nominal contact face carries compressive stress. Following the numerical observations in Fig. 5, the time-dependent trailing-to-leading stress ratio is replaced by a representative constant c within each contact transition. The linear distribution can therefore be expressed as

$$\sigma_n(\xi, t) = \sigma_B(t)\left[c + (1-c)\frac{\xi}{l_b}\right], \qquad 0 \le \xi \le l_b, \tag{5}$$

where $\sigma_A(t) = c\sigma_B(t)$. This approximation fixes the normalized spatial profile while allowing the amplitude $\sigma_B(t)$ to evolve during the transition. Thus, the full-contact stress distribution is simply described by c and $\sigma_B(t)$ without explicitly resorting to the complex stress field in the contact region.

To evaluate the contact moments analytically, the moment arms are approximated by those at the nominal configuration in which the contact face is parallel to the supporting plane. Neglecting the small configuration changes during an individual transition gives $x(\xi, t) - x(t) \approx \xi - l_b/2$. Integrating Eq. (5) along the contact face, consistently with the contact integrals in Section 2.2 and the axial-integration convention above, gives $F_{cy}(t) = g_1\sigma_B(t)$ and $M_{cy}(t) = g_2\sigma_B(t)$, where

$$\begin{cases} g_1 = \dfrac{1}{2}(1+c)l_b, \\ g_2 = \dfrac{1}{12}(1-c)l_b^2. \end{cases} \tag{6}$$

The coefficients g_1 and g_2 relate the leading-edge line load to the normal contact resultant and its moment about the centroid, respectively.

Based on the analysis in the preceding section, when the number of edges is sufficiently large and the coefficient of friction is large enough, the tangential interaction will remain in the stick regime, and the tangential-force coefficient g_3 will take the

following form

$$g_3 = -\frac{mr\cos\alpha}{J + mr^2\cos^2\alpha}\, g_2. \tag{7}$$

Then, the prism contact dynamics equation can be written as

$$\begin{cases} m\ddot{x} = g_3\sigma_B(t), \\ m\ddot{y} = g_1\,\sigma_B(t) - F_{py}, \\ J\ddot{\theta} = (g_2 + r\cos\alpha\, g_3)\sigma_B(t). \end{cases} \tag{8}$$

Because the contact duration is short and difficult to determine directly, an impulse formulation is adopted. Here, by defining the stress impulse at point B as $dp^* = \sigma_B(t)\,\mathrm{d}t$, the equations of motion in Eq. (8) can be recast in differential impulse form

$$\begin{cases} m\,d\dot{x} = g_3 dp^*, \\ m\,\mathrm{d}\dot{y} = g_1 dp^* - \mathrm{d}I_L, \\ J\mathrm{d}\dot{\theta} = (g_2 + rg_3\cos\alpha)\,\mathrm{d}p^*, \end{cases} \tag{9}$$

where $dI_L = F_{py}\mathrm{d}t$ is the differential load impulse accumulated during the contact interval. Let $\dot{x}^-, \dot{y}^-$ and $\dot{\theta}^-$ be the translational and rotational velocities just before contact at time t^-. Correspondingly, let $\dot{x}^+, \dot{y}^+$ and $\dot{\theta}^+$ be the translational and rotational velocities at time t^+, after the contact has completed. Furthermore, defining p^* as the total impulse of point B over the interval from t^- to t^+, the velocity difference of the prism before and after contact can be written as

$$\begin{cases} \dot{x}^+ - \dot{x}^- = \dfrac{g_3}{m}\, p^*, \\ \dot{y}^+ - \dot{y}^- = \dfrac{g_1}{m}\, p^* - \dfrac{I_L}{m}, \\ \dot{\theta}^+ - \dot{\theta}^- = \dfrac{g_2 + rg_3\cos\alpha}{J}\, p^*, \end{cases} \tag{10}$$

where I_L is the external load impulse during the contact process.

Assuming that each edge undergoes a complete compression–release cycle during a contact transition, the contact duration for sufficiently large N is approximated by the time required for the prism to rotate through an angle 2α. Thus, the contact time can be estimated as $\Delta t = \frac{2\alpha}{|\dot{\theta}^-|}$, which is $\Delta t = -\frac{2\alpha}{\dot{\theta}^-}$ when the prism rolls in the positive x-direction. Therefore, the external force impulse during impact can be calculated as:

$$I_L = F_{py}\Delta t = -\frac{2F_{py}\alpha}{\dot{\theta}^-}. \tag{11}$$

The translational and rotational velocity transformations in Eq. (10) are not independent; they must satisfy certain kinematic constraints. First, before switching state occurs, the prism rotates about point A; therefore, the normal velocity of point B is

$v_{Bn}(t^-) = 2r\sin\alpha\,\dot{\theta}^-$. Second, once the contact is completed, the prism rotates about point B; hence, the normal velocity of point B becomes $v_{Bn}(t^+) = 0$. Moreover, from the centroid kinematics, the normal velocity of point B just before contact, $v_{Bn}(t^-)$, and after contact has been completed, $v_{Bn}(t^+)$, can be calculated as

$$\begin{cases} v_{Bn}(t^-) = \dot{y}^- + r\sin\alpha\,\dot{\theta}^- = 2r\sin\alpha\,\dot{\theta}^-, \\ v_{Bn}(t^+) = \dot{y}^+ + r\sin\alpha\,\dot{\theta}^+ = 0. \end{cases} \tag{12}$$

By combining Eq. (10) and Eq. (12) p^* can be determined as

$$p^* = \frac{\dfrac{1}{m}I_L - 2r\sin\alpha\,\dot{\theta}^-}{\dfrac{g_1}{m} + \dfrac{g_2 + rg_3\cos\alpha}{J}r\sin\alpha} \tag{13}$$

Substituting Eq. (13) into the rotational jump relation in Eq. (10) gives

$$\dot{\theta}^+ = R_\omega\dot{\theta}^- - R_L\frac{F_{py}}{\dot{\theta}^-}, \tag{14}$$

where

$$\begin{cases} R_\omega = \dfrac{Jg_1 - (g_2 + rg_3\cos\alpha)mr\sin\alpha}{Jg_1 + (g_2 + rg_3\cos\alpha)mr\sin\alpha}, \\ R_L = \dfrac{2\alpha(g_2 + rg_3\cos\alpha)}{Jg_1 + (g_2 + rg_3\cos\alpha)mr\sin\alpha}. \end{cases} \tag{15}$$

Here, R_ω is the angular-velocity transmission coefficient, and R_L is the external load coefficient.

3.2 From line impact to rolling resistance

Based on the prism contact dynamics derived above, we next construct an equivalent rolling-resistance model for a cylindrical body using a large-edge-number approximation. We begin with the energy loss associated with each contact transition.

At each impact, the loss in kinetic energy can be calculated as

$$\Delta T = \frac{1}{2}(J + mr^2)\left[\left(\dot{\theta}^-\right)^2 - \left(\dot{\theta}^+\right)^2\right]. \tag{16}$$

In this period, the prism rotates through an angle $2\alpha = \frac{2\pi}{N}$. In this process, by introducing a rolling-resistance moment denoted as M_d, the work done by M_d is $M_d 2\alpha$, which should equal the total energy dissipation ΔT. Thus, we can obtain

$$M_d = \frac{\Delta T}{2\alpha} = \frac{N}{2\pi}\cdot\frac{1}{2}(J + mr^2)\left[\left(\dot{\theta}^-\right)^2 - \left(\dot{\theta}^+\right)^2\right]. \tag{17}$$

Substituting Eq. (14) into Eq. (17) yields

$$M_d = \frac{N(J+mr^2)}{4\pi}\left[\left(1-R_\omega^2\right)\left(\dot{\theta}^-\right)^2 + 2R_\omega R_L F_{py} - \left(\frac{R_L F_{py}}{\dot{\theta}^-}\right)^2\right]. \tag{18}$$

Next, we focus on the simplified forms of these combination coefficients when N is sufficiently large. In this case, we have $\sin\alpha \sim \frac{\pi}{N}, \cos\alpha \sim 1$. Using these approximations and combining Eqs. (6), (7) and (15), we can simplify the corresponding coefficients of M_d as $M_d = M_1 + M_2 + M_3$, where

$$\begin{cases} M_1 = \dfrac{N(J+mr^2)(1-R_\omega^2)}{4\pi} \approx \dfrac{mr^2(1-c)}{3(1+c)}\dfrac{\pi}{N}, \\ M_2 = \dfrac{2N(J+mr^2)R_\omega R_L F_{py}}{4\pi} \approx \dfrac{(1-c)F_{py}r}{3(1+c)}\dfrac{\pi}{N}, \\ M_3 = -\dfrac{N(J+mr^2)}{4\pi}F_{py}^2 R_L^2 \approx -\dfrac{F_{py}^2 r^2(1-c)^2}{9(J+mr^2)(1+c)^2}\dfrac{\pi^3}{N^3}. \end{cases} \tag{19}$$

It is observed that both M_1 and M_2 scale linearly with $\frac{\pi}{N}$, whereas M_3 exhibits a cubic dependence on $\frac{\pi}{N}$. Since $\frac{\pi^3}{N^3} \ll \frac{\pi}{N}$, the contribution of the term M_3 can be neglected. Thus, the rolling-resistance moment M_d can be reduced to

$$M_d = M_1\dot{\theta}^2 + M_2 = \frac{\pi(1-c)mr^2}{3N(1+c)}\dot{\theta}^2 + \frac{\pi(1-c)r}{3N(1+c)}F_{py}. \tag{20}$$

It is shown that rolling resistance decreases as the number of edges N increases. In particular, as $N \to \infty$, the rolling resistance approaches zero. This behavior is consistent with the physical principle that ideal rigid-body contacts do not involve energy dissipation.

When the load is small and the rolling speed is high, the load-dependent terms in Eq.(20) can be neglected. In this case, the rolling resistance becomes proportional to the square of the rolling speed, which is consistent with the theoretical model built in [12]. Conversely, for the low-speed and heavy-load conditions addressed in this study, the velocity-dependent term in Eq.(20) is negligible, and the equation simplifies to

$$M_d = \frac{\pi(1-c)r}{3N(1+c)}F_{py}. \tag{21}$$

This form exhibits the same characteristic load–contact-width dependence as Greenwood's classical hysteretic rolling-resistance model, $M_d = \alpha_G F_{py} b/(3\pi)$, once the prism edge length is related to the cylindrical contact width. In Greenwood's model, b denotes the full contact width, and α_G represents the energy loss coefficient associated with material hysteresis. In the present model, the number of prism edges N characterizes the effective contact size, whereas c describes the trailing-to-leading normal-stress ratio.

To establish this geometric correspondence, the side length of the equivalent prism is identified with the full Hertzian contact width of the cylinder. By applying Hertzian

line-contact theory, the full contact width b under the total normal load F_{py} is obtained as

$$b = 4\left(\frac{F_{py}r}{\pi l E^*}\right)^{1/2}, \tag{22}$$

where l is the axial contact length and E^* is the equivalent contact modulus, defined by $1/E^* = (1-\nu_1^2)/E_1 + (1-\nu_2^2)/E_2$. Here, E_1 and E_2 are the Young's moduli of the cylinder and the supporting plane, respectively, and ν_1 and ν_2 are their corresponding Poisson's ratios.

The geometric mapping is illustrated in Fig. 6. The cylindrical contact in Fig. 6(a) has a finite width b, which is represented by the side length l_b of the equivalent regular prism in Fig. 6(b). Thus, $l_b = b$. This mapping preserves the characteristic contact width without requiring identical local pressure distributions.

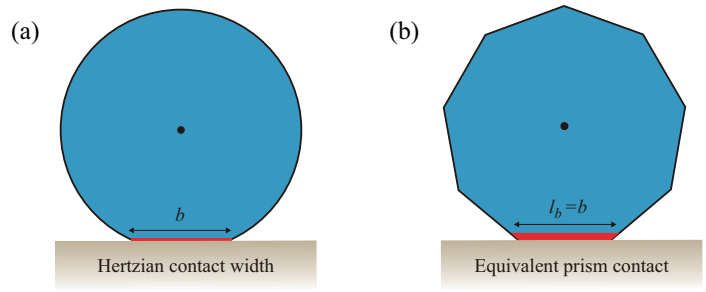


Fig. 6 Geometric mapping based on the Hertzian contact width: (a) cylindrical contact with full Hertzian contact width b; (b) an equivalent regular prism with side length $l_b = b$. The contact regions are highlighted in red. The deformation and polygon size are exaggerated for clarity.

Denoting the equivalent number of prism edges by N_{eq}, the geometric relation is $b = l_b = 2r\sin(\pi/N_{\mathrm{eq}})$. For sufficiently large N_{eq}, this relation reduces to $b \approx 2\pi r/N_{\mathrm{eq}}$, giving $N_{\mathrm{eq}} \approx 2\pi r/b$. Combining this approximation with Eq. (22), the equivalent number of prism edges accounting for the finite cylindrical contact width is obtained as

$$N_{\mathrm{eq}} \approx \frac{\pi r}{2}\left(\frac{\pi l E^*}{F_{py}r}\right)^{1/2}. \tag{23}$$

By substituting Eq. (23) into Eq. (21), the rolling-resistance moment accounting for local cylindrical contact deformation can be expressed as

$$M_d = \frac{2(1-c)}{3(1+c)}\left(\frac{F_{py}r}{\pi l E^*}\right)^{1/2} F_{py}. \tag{24}$$

4 Results and Discussion

This section will assesse the proposed rolling-resistance formulation from two directions. It first identifies the effective stress-asymmetry parameter from the experiments of Kumar et al. [94] and examines the macroscopic scaling predicted by the model. It

then compares the formulation with Greenwood's classical hysteretic model to assess its consistency with an established energy-loss description.

4.1 Experimental identification and scaling comparison

The rolling-resistance experiments reported by Kumar et al. [94] include Teflon, PMMA, and steel wheels under different combinations of wheel radius and normal load, while the reported rolling velocities remain relatively low. These experiments therefore provide a suitable dataset for examining the effective stress-asymmetry parameter c within the high-load rolling regime considered in the resent formulation.

For each experimental condition, the cylindrical wheel is represented by an equivalent regular prism using the Hertzian line-contact width derived in Section 3. The analytical energy loss is applied at each leading edge transition in the discrete prism-rolling model, while fixed-point rotation is retained between adjacent transitions. An equivalent horizontal driving force corresponding to the experimentally inferred rolling resistance is introduced, and c is adjusted until the long-term numerical rolling velocity reproduces the experimentally reported average value. As a representative example, Case 14 corresponds to a PMMA wheel with $r = 72.0$ mm and $N' = 40.29$ kN/m. The Hertzian contact width gives $N_{\mathrm{eq}} = 261$, and the identified stress-asymmetry parameter is $c = 0.648$.

The same procedure was subsequently applied to all 22 experimental cases. Fig. 7 shows the identified values of c in relation to the experimentally reported average rolling velocity and the normal load per unit axial width.

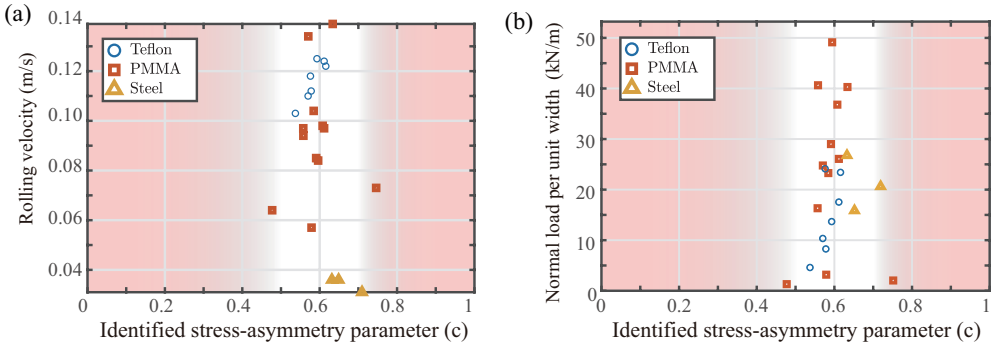


Fig. 7 Identified stress-asymmetry parameter c for the 22 rolling-resistance experiments reported by Kumar et al. [94]: (a) relationship with the experimentally reported average rolling velocity and (b) relationship with the normal load per unit axial width. Different symbols denote the three wheel materials.

As shown in Fig. 7, the identified values of c remain relatively concentrated despite substantial variations in wheel material,geometry, normal load, and rolling velocity. The mean value over the 22 cases is approximately 0.61, and 17 cases fall within the interval $0.55 < c < 0.65$. No systematic monotonic dependence of c on either the reported average rolling velocity or the normal load is evident over the investigated range. Although some scatter remains among individual cases and materials,

the overall distribution is centered near $c \simeq 0.6$. Accordingly, $c = 0.6$ is adopted as a representative reference value for comparable low-speed and heavy-load rolling conditions, while case-specific adjustment may be introduced when more detailed contact information is available.

The high-load character of these experimental conditions can also be quantified from the two contributions in Eq. (20). For all 22 cases, the ratio of the velocity-dependent contribution to the load-dependent contribution remains below approximately 3.1%. The inertial contribution is therefore limited over the experimental range considered, supporting the low-speed approximation employed in the present formulation.

The macroscopic scaling predicted by the present formulation can further be compared with that reported by Kumar et al. [94]. Their energy model was correlated through the dimensionless elastic-contact parameter $\Omega = N'/(ER)$ and yielded a power-law exponent of approximately 0.48, with the numerical predictions showing good correspondence with the experimental results. In the low-speed limit, the rolling resistance μ_{rr} can be defined as

$$\mu_{rr} \propto \left(\frac{N'}{E^* r}\right)^{1/2}. \tag{25}$$

The corresponding exponent of 0.5 is close to that obtained by Kumar et al., indicating a similar dependence of rolling resistance on normal load, elastic stiffness, and wheel radius.

4.2 Comparison with Greenwood's rolling-resistance model

The low-speed form of the present formulation is further compared with Greenwood's classical hysteretic rolling-resistance model [12]. For a hard cylinder of radius r rolling on a deformable plane under a normal load F_{py}, Greenwood assumes that the rolling resistance is dominated by material hysteresis, that interfacial slip and adhesion are negligible, and that the contact pressure follows the static Hertz distribution. Within this framework, the energy loss per unit rolling distance is obtained by integrating, over the depth of the elastic half-space, the hysteresis loss associated with the length of the local stress path. For a long cylinder, this procedure yields a resisting moment $M_d = \frac{\alpha_G F_{py} b}{3\pi}$, where b is the full Hertzian contact width and α_G denotes the fraction of the elastic input energy dissipated through material hysteresis. Their subsequent treatment of complex deformation cycles modifies the numerical coefficient while retaining the characteristic dependence on normal load and contact width. Within the low-speed, high-load regime considered here, the present formulation gives $M_d \simeq [(1-c)/(6(1+c))]F_{py}b$. Both descriptions therefore yield $M_d \propto F_{py}b$, with the dependence on radius and elastic properties entering through the contact width. Their coefficients represent different aspects of the local contact process: the hysteretic formulation characterizes energy losses during material deformation, whereas c represents the effective normal-stress asymmetry in the present contact-dynamics formulation.

For the long-cylinder configuration, Greenwood et al. obtained $\mu_{\mathrm{rr}} \simeq 0.06a/r$, where $a = b/2$ is the contact half-width, and reported close agreement with their long-cylinder experimental results. The corresponding low-speed expression of the present model is $\mu_{\mathrm{rr}} = [(1-c)/(3(1+c))]a/r$. Equating the two expressions gives an equivalent parameter $c_{G,\mathrm{eq}} \simeq 0.695$. This value lies within the broader interval $0.5 < c < 0.7$ and is comparable with the characteristic magnitude identified in Section 4.1, although it is above the principal concentration interval of $0.55 < c < 0.65$. This correspondence concerns the macroscopic resistance coefficient and does not constitute a direct measurement of the contact-stress ratio.

The possible magnitude of the velocity-dependent contribution can also be assessed through a conditional estimate. Greenwood et al. reported an oscillation period of $T = 6$ s for a pendulum-based rolling experiment, but did not provide sufficient amplitude information to determine its rolling speed. Assuming approximately sinusoidal horizontal motion with a single-sided displacement amplitude u_0, the peak rolling speed is $v_{\max} = 2\pi u_0/T$. For an assumed amplitude of $u_0 = 5$ mm, this gives $v_{\max} \simeq 5.24 \times 10^{-3}$ m/s.

From Eq. (20), the ratio of the velocity-dependent contribution M_v to the load-dependent contribution M_P is $M_v/M_P = mv^2/(rF_{py})$. Using a representative radius of $r = 25$ mm and, for this illustrative estimate, $F_{py} = mg$, the peak ratio is approximately 1.12×10^{-4}, or 0.011%. For assumed amplitudes between 1 and 10 mm, the peak ratio remains below 0.05%. Thus, the velocity-dependent contribution is negligible under these estimated conditions. The selected radius, amplitude, and mass–load relation are not a reconstruction of the reported pendulum apparatus; this calculation provides a magnitude estimate rather than a quantitative validation against a specific experimental condition.

The comparison consequently supports consistency in the functional structure and characteristic magnitude of the load-dependent rolling resistance. The equivalent value of c and the conditional velocity estimate are compatible with the reduced description adopted here, without implying equivalence between the underlying local dissipation mechanisms.

5 Conclusions

This study develops an analytical rolling-resistance model for a cylinder under low-speed and heavy-load conditions by representing the cylindrical contact through an equivalent regular prism. Starting from the repeated line-contact dynamics of the prism, the mechanical-energy loss associated with each edge transition is converted into an equivalent continuous rolling-resistance moment. Under the Case-II contact condition with an approximately constant stress-asymmetry parameter c, the resulting resistance consists of a load-dependent contribution and a velocity-dependent contribution proportional to the square of the angular velocity. By relating the prism edge length to the Hertzian line-contact width, the formulation further incorporates the effects of normal load, rolling radius, elastic stiffness, and contact-stress asymmetry.

Numerical contact analysis shows that Case-II contact is maintained over the relatively low-speed range considered and that the stress ratio varies only slightly over

most of an individual contact event, supporting the assumptions used in the analytical reduction. Evaluation using the 22 rolling-resistance experiments reported by Kumar et al. shows that the identified values of c are concentrated around $c \simeq 0.6$, while the velocity-dependent contribution remains small relative to the load-dependent term. The resulting low-speed scaling, $\mu_{rr} \propto [N'/(E^* r)]^{1/2}$, is also close to the 0.48 power-law dependence reported in Kumar's energy model. In addition, comparison with Greenwood's classical hysteretic formulation shows that both models recover the same characteristic dependence $F_{rr} \propto F_{py} b/r$ in the low-speed limit, despite their different descriptions of the local dissipation process.

The present formulation is primarily applicable to rolling conditions for which the contact remains in Case-II, the stress asymmetry can be approximated as nearly constant, and the effective contact width remains small relative to the cylinder radius. At higher rolling velocities, the transition toward Case-I and the stronger temporal variation of the contact stress may require the contact-boundary evolution to be retained explicitly. The current model also does not explicitly include strongly non-Hertzian contact, pronounced three-dimensional effects, local slip, or rate-dependent material dissipation. Incorporating these effects provides a possible route for extending the present contact-dynamics framework to a broader range of rolling conditions.

Declarations

This work is supported by the National Science Foundation of China under Contract Nos.12672051

References

[1] Hall, D.E., Moreland, J.C.: Fundamentals of rolling resistance. Rubber chemistry and technology **74**(3), 525–539 (2001)

[2] Qiu, X.: Full two-dimensional model for rolling resistance: hard cylinder on viscoelastic foundation of finite thickness. Journal of Engineering Mechanics **132**(11), 1241–1251 (2006)

[3] Taoka, Y., Watanabe, T., Iguchi, Y., Hemthavy, P., Takahashi, K., Saito, S.: Adhesional rolling behavior of micro-cylinder: Experimental observation of adhesional contacts and measurement of critical rolling resistance. Journal of Physics Communications **4**(12), 125002 (2020)

[4] Saito, S., Ochiai, T., Yoshizawa, F., Dao, M.: Rolling behavior of a micro-cylinder in adhesional contact. Scientific Reports **6**(1), 34063 (2016)

[5] Offner, D., Tomita, N.: Determining the coefficient of friction for rolling disks (1978)

[6] Duda, S., Gembalczyk, G., Machoczek, T., Kowalik, Z.: Experimental evaluation of rolling resistance in omnidirectional wheels under quasi-static conditions.

Sensors **25**(16), 5026 (2025)

[7] Juliá, J.M., Rodríguez-Tembleque, L.: Wear and subsurface stress evolution in tractive rolling contact. International Journal of Mechanical Sciences **294**, 110195 (2025)

[8] Nanayakkara, S., Zhao, J., Terrington, S., Thompson, M., Hourigan, K.: Effects of surface roughness on the drag coefficient of finite-span cylinders freely rolling on an inclined plane. Journal of Fluid Mechanics **998**, 39 (2024)

[9] Reynolds, O.: Vi. on rolling-friction. Philosophical Transactions of the Royal Society of London (166), 155–174 (1876)

[10] Johnson, K.L.: One hundred years of hertz contact. Proceedings of the Institution of Mechanical Engineers **196**(1), 363–378 (1982)

[11] Fischer-Cripps, A.: The hertzian contact surface. Journal of materials science **34**(1), 129–137 (1999)

[12] Greenwood, J., Minshall, H., Tabor, D.: Hysteresis losses in rolling and sliding friction. Proceedings of the Royal Society of London. Series A. Mathematical and Physical Sciences **259**(1299), 480–507 (1961)

[13] Tabor, D.: The mechanism of rolling friction. The London, Edinburgh, and Dublin Philosophical Magazine and Journal of Science **45**(369), 1081–1084 (1954)

[14] Hunter, S.: The rolling contact of a rigid cylinder with a viscoelastic half space (1961)

[15] Morland, L.: Rolling contact between dissimilar viscoelastic cylinders. Quarterly of Applied Mathematics **25**(4), 363–376 (1968)

[16] Morland, L.: A plane problem of rolling contact in linear viscoelasticity theory (1962)

[17] Tiwari, A., Miyashita, N., Persson, B.N.: Rolling friction of elastomers: role of strain softening. Soft matter **15**(45), 9233–9243 (2019)

[18] Zhang, P., Morris, M., Doshi, D.: Materials development for lowering rolling resistance of tires. Rubber Chemistry and Technology **89**(1), 79–116 (2016)

[19] Buezas, F.S., Fochesatto, N.S.: Power dissipation of a viscoelastic rolling wheel in finite deformations. International Journal of Mechanical Sciences **138**, 502–514 (2018)

[20] Wallace, E.R., Chaise, T., Nelias, D.: Three-dimensional rolling/sliding contact on a viscoelastic layered half-space. Journal of the Mechanics and Physics of Solids **143**, 104067 (2020)

[21] Persson, B.: Rolling friction for hard cylinder and sphere on viscoelastic solid. The European Physical Journal E **33**(4), 327–333 (2010)

[22] Carbone, G., Putignano, C.: A novel methodology to predict sliding and rolling friction of viscoelastic materials: Theory and experiments. Journal of the Mechanics and Physics of Solids **61**(8), 1822–1834 (2013)

[23] Menga, N., Bottiglione, F., Carbone, G.: The indentation rolling resistance in belt conveyors: A model for the viscoelastic friction. Lubricants **7**(7), 58 (2019)

[24] Liang, X.-M., Ding, Y., Li, C.-Y., Wang, G.-F.: An incremental contact model for rough viscoelastic solids. International Journal of Mechanical Sciences **255**, 108483 (2023)

[25] Zhang, X., Wang, Q.J., He, T.: Transient and steady-state viscoelastic contact responses of layer-substrate systems with interfacial imperfections. Journal of the Mechanics and Physics of Solids **145**, 104170 (2020)

[26] Santeramo, M., Putignano, C., Vorlaufer, G., Krenn, S., Carbone, G.: Viscoelastic steady-state rolling contacts: A generalized boundary element formulation for conformal and non-conformal geometries. Journal of the Mechanics and Physics of Solids **171**, 105129 (2023)

[27] Marshall, E.: Rolling contact with plastic deformation. Journal of the Mechanics and Physics of Solids **16**(4), 243–254 (1968)

[28] Berthe, L., Sainsot, P., Lubrecht, A., Baietto, M.-C.: Plastic deformation of rough rolling contact: An experimental and numerical investigation. Wear **312**(1-2), 51–57 (2014)

[29] Drutowski, R.: The role of microslip for freely rolling bodies (1965)

[30] Afferrante, L.: Winkler partial slip solution for harmonic oscillations in steady rolling contact problems. International Journal of Solids and Structures **45**(22-23), 5962–5971 (2008)

[31] Wilson, R., Dini, D., Van Wachem, B.: The influence of surface roughness and adhesion on particle rolling. Powder technology **312**, 321–333 (2017)

[32] Bentall, R., Johnson, K.: Slip in the rolling contact of two dissimilar elastic rollers. International journal of mechanical sciences **9**(6), 389–404 (1967)

[33] Violano, G., Afferrante, L.: On the contact between elasto-plastic media with self-affine fractal roughness. International Journal of Mechanical Sciences **255**, 108461 (2023)

[34] Fu, P., Zhao, J., Zhang, X., Miao, H., Wen, Z., Wang, P., Kang, G., Kan, Q.: Elasto-plastic partial slip contact modeling of graded layers. International Journal

of Mechanical Sciences **264**, 108823 (2024)

[35] Chen, Y., Zhang, M., Wang, Q.J.: Analysis of adhesive contact of heterogeneous elastic materials. International Journal of Mechanical Sciences **266**, 108986 (2024)

[36] Menga, N., Carbone, G., Dini, D.: Exploring the effect of geometric coupling on friction and energy dissipation in rough contacts of elastic and viscoelastic coatings. Journal of the Mechanics and Physics of Solids **148**, 104273 (2021)

[37] Xu, Y., Scheibert, J., Gadegaard, N., Mulvihill, D.M.: An asperity-based statistical model for the adhesive friction of elastic nominally flat rough contact interfaces. Journal of the Mechanics and Physics of Solids **164**, 104878 (2022)

[38] Ceglie, M., Violano, G., Afferrante, L., Menga, N.: Finite deformations induce friction hysteresis in normal wavy contacts. International Journal of Mechanical Sciences **291**, 110115 (2025)

[39] Karttunen, A.T., Hertzen, R.: Dynamic response of a cylinder cover under a moving load. International Journal of Mechanical Sciences **82**, 170–178 (2014)

[40] Yang, Z., Li, Z.: A numerical study on waves induced by wheel-rail contact. International Journal of Mechanical Sciences **161**, 105069 (2019)

[41] Yang, Z., Li, Z., Dollevoet, R.: Modelling of non-steady-state transition from single-point to two-point rolling contact. Tribology International **101**, 152–163 (2016)

[42] Bogacz, R.: Dynamic analysis of rolling contact problem by the space-time element method. ZAMM. Z. Angew. Math. Mech **80**, 1 (2000)

[43] Ydrefors, L., Hjort, M., Kharrazi, S., Jerrelind, J., Stensson Trigell, A.: Rolling resistance and its relation to operating conditions: A literature review. Proceedings of the Institution of Mechanical Engineers, Part D: Journal of Automobile Engineering **235**(12), 2931–2948 (2021)

[44] Narasimha Rao, K., Kumar, R.K., Bohara, P.: A sensitivity analysis of design attributes and operating conditions on tyre operating temperatures and rolling resistance using finite element analysis. Proceedings of the Institution of Mechanical Engineers, Part D: Journal of Automobile Engineering **220**(5), 501–517 (2006)

[45] Aldhufairi, H.S., Olatunbosun, O.A.: Developments in tyre design for lower rolling resistance: A state of the art review. Proceedings of the Institution of Mechanical Engineers, Part D: Journal of Automobile Engineering **232**(14), 1865–1882 (2018)

[46] Ejsmont, J., Taryma, S., Ronowski, G., Swieczko-Zurek, B.: Influence of load and inflation pressure on the tyre rolling resistance. International journal of automotive technology **17**(2), 237–244 (2016)

[47] Ejsmont, J.A., Ronowski, G., Świeczko-Żurek, B., Sommer, S.: Road texture influence on tyre rolling resistance. Road Materials and Pavement Design **18**(1), 181–198 (2017)

[48] Ilse, M., *et al.*: Evaluation of tire/surfacing/base contact stresses and texture depth. International Journal of Transportation Science and Technology **4**(1), 107–118 (2015)

[49] Nowell, D., Hills, D.: Tractive rolling of dissimilar elastic cylinders. International journal of mechanical sciences **30**(6), 427–439 (1988)

[50] Meymand, S.Z., Keylin, A., Ahmadian, M.: A survey of wheel–rail contact models for rail vehicles. Vehicle System Dynamics **54**(3), 386–428 (2016)

[51] Montenegro, P., Calçada, R.: Wheel–rail contact model for railway vehicle–structure interaction applications: development and validation. Railway Engineering Science **31**(3), 181–206 (2023)

[52] Xia, F., Cole, C., Wolfs, P.: The dynamic wheel–rail contact stresses for wagon on various tracks. Wear **265**(9-10), 1549–1555 (2008)

[53] Polach, O.: Creep forces in simulations of traction vehicles running on adhesion limit. Wear **258**(7-8), 992–1000 (2005)

[54] Grassie, S.L., Elkins, J.A.: Tractive effort, curving and surface damage of rails: Part 1. forces exerted on the rails. Wear **258**(7-8), 1235–1244 (2005)

[55] Zhai, W., Wang, K., Cai, C.: Fundamentals of vehicle–track coupled dynamics. Vehicle System Dynamics **47**(11), 1349–1376 (2009)

[56] Vo, K., Tieu, A.K., Zhu, H., Kosasih, P.B.: A 3d dynamic model to investigate wheel–rail contact under high and low adhesion. International Journal of Mechanical Sciences **85**, 63–75 (2014)

[57] Jin, X., Li, X., Bai, L., Guo, F., Gao, J., Poll, G.: Effect of contact geometry on lubricant replenishment in grease lubricated rolling contacts. Tribology International **200**, 110077 (2024)

[58] Houpert, L., Clarke, J., Penny, C.: Tribological models for advanced ball bearing simulation. Tribology Transactions **66**(4), 645–660 (2023)

[59] Sakhamuri, M.S.D., Harvey, T.J., Vierneusel, B., Wood, R.J.: Wear induced changes in surface topography during running-in of rolling-sliding contacts. Wear **522**, 204685 (2023)

[60] Lorenz, S.J., Sadeghi, F., Trivedi, H.K., Rosado, L., Kirsch, M.S., Wang, C.: A continuum damage mechanics finite element model for investigating effects of surface roughness on rolling contact fatigue. International Journal of Fatigue **143**, 105986 (2021)

[61] Terwisscha-Dekker, H., Brouwer, A.M., Weber, B., Bonn, D.: Elastic contact between rough surfaces: Bridging the gap between theory and experiment. Journal of the Mechanics and Physics of Solids **188**, 105676 (2024)

[62] Hu, H., Batou, A., Ouyang, H.: An isogeometric analysis based method for frictional elastic contact problems with randomly rough surfaces. Computer Methods in Applied Mechanics and Engineering **394**, 114865 (2022)

[63] Aimi, A., Di Credico, G., Gimperlein, H.: Time domain boundary elements for elastodynamic contact. Computer Methods in Applied Mechanics and Engineering **415**, 116296 (2023)

[64] Monti, J.M., Pastewka, L., Robbins, M.O.: Fractal geometry of contacting patches in rough elastic contacts. Journal of the Mechanics and Physics of Solids **160**, 104797 (2022)

[65] Gargourimotlagh, M., Rooij, M.: The effect of highly elongated micro-contacts on rolling contact stress field. Tribology international **196**, 109744 (2024)

[66] Rango, I.E., Buezas, F.S., Prieto, G., Failla, M.: Hysteretic friction in elastomer-rough surface contacts: A continuum mechanics approach without empirical parameters. International Journal of Mechanical Sciences, 111305 (2026)

[67] Guler, M., Alinia, Y., Adibnazari, S.: On the rolling contact problem of two elastic solids with graded coatings. International Journal of Mechanical Sciences **64**(1), 62–81 (2012)

[68] Stiebritz, C., Hai-Ping, Y., Cesbron, J.: Single level fast multipole method for frictionless rough contact problems. International Journal of Mechanical Sciences **286**, 109810 (2025)

[69] Bürger, L., Boukadia, R., Naets, F.: A reduced order modeling strategy for nonlinear elasto-dynamic systems with cyclic symmetry in rolling contact. Journal of Sound and Vibration, 119645 (2026)

[70] Pawar, G.S., Kulkarni, S.S.: Efficient parametric model order reduction in contact mechanics. Computers & Structures **315**, 107838 (2025)

[71] Zhang, S., Devriendt, H., Van Belle, L., Desmet, W.: Substructuring-based parametric reduced-order modelling for structural dynamic predictions of bolted assemblies. Mechanical Systems and Signal Processing **218**, 111513 (2024)

[72] Li, C., Yang, Z., Chen, Z., Jia, T.: Blade reduced model considering local contact and analyzing blade vibration characteristics. Journal of Sound and Vibration **557**, 117772 (2023)

[73] Deng, Y., Wang, Z., Shen, H., Gong, J., Xiao, Z.: A comprehensive review on non-pneumatic tyre research. Materials & Design **227**, 111742 (2023)

[74] Liu, S., Liu, W., Zhou, S., Li, X., Zhang, Q.: Steady-state temperature field and rolling resistance characteristics of low-speed and low-load capacity non-pneumatic tires. Lubricants **11**(9), 402 (2023)

[75] Hyttinen, J., Rothhämel, M., Jerrelind, J., Drugge, L.: Simulation of transient rolling resistance of bicycle tyres at various ambient temperatures. PloS one **19**(6), 0302821 (2024)

[76] Chen, D., Wu, J., Su, B., Cui, B., Teng, F., An, S., Bai, Y., Liu, X., Liu, Y., Wang, Y.: Thermo-mechanical-abrasive coupling analysis of solid rubber tire under high-speed rolling. Wear **512**, 204546 (2023)

[77] Wu, A., Zhang, Z., Shi, X., Liu, C.: Modeling the role of interfacial adhesion in the rolling resistance of a hyperelastic wheel. Tribology International **185**, 108494 (2023)

[78] Sina, N., Nasiri, S., Karkhaneh, V.: Effects of resistive loads and tire inflation pressure on tire power losses and co2 emissions in real-world conditions. Applied Energy **157**, 974–983 (2015)

[79] Mandriota, C., Menga, N., Carbone, G.: Enhancement of adhesion strength in viscoelastic unsteady contacts. Journal of the Mechanics and Physics of Solids **192**, 105826 (2024)

[80] Vlachakis, G., Colombo, C., Giouvanidis, A.I., Lourenço, P.B.: Generalised kinematic single-impact and multi-impact models for rocking structures. Earthquake Engineering & Structural Dynamics **55**(6), 1179–1202 (2026)

[81] Várkonyi, P.L., Kocsis, M., Ther, T.: Rigid impacts of three-dimensional rocking structures. Nonlinear Dynamics **107**(3), 1839–1858 (2022)

[82] Zhu, H., Chatzis, M.N., Acikgoz, S.: A new impact model for the flexible rocking oscillator. Earthquake Engineering & Structural Dynamics **51**(8), 1819–1839 (2022)

[83] Bao, Y.: A distributed impact model for seismic analysis of planar rocking body. Journal of Earthquake Engineering **28**(10), 2781–2800 (2024)

[84] Ding, S., Wan, Z., Zhang, Y., Hu, Y., Xia, R., Hu, G.: Analytical coefficient of restitution model linking viscoelasticity and improved contact force model.

International Journal of Mechanical Sciences **299**, 110388 (2025)

[85] Zhao, Z., Liu, C., Ma, D.: Pure rotation of a prism on a ramp. Proceedings of the Royal Society A: Mathematical, Physical and Engineering Sciences **470**(2169), 20140007 (2014)

[86] Zhao, Z., Wang, N., Liu, C.: Jump rule for edge impacts of rolling prisms. Theoretical and Applied Mechanics Letters **8**(6), 425–430 (2018)

[87] Zhao, X., Meng, W., Zhou, L.: Indentation rolling resistance based on a three-parameter kelvin solid model. Advances in Mechanical Engineering **11**(4), 1687814019839517 (2019)

[88] Leine, R.I.: Experimental and theoretical investigation of the energy dissipation of a rolling disk during its final stage of motion. Archive of Applied Mechanics **79**(11), 1063–1082 (2009)

[89] Easwar, K., Rouyer, F., Menon, N.: Speeding to a stop: the finite-time singularity of a spinning disk. Physical Review E **66**(4), 045102 (2002)

[90] Caps, H., Dorbolo, S., Ponte, S., Croisier, H., Vandewalle, N.: Rolling and slipping motion of euler's disk. Physical Review E—Statistical, Nonlinear, and Soft Matter Physics **69**(5), 056610 (2004)

[91] Le Saux, C., Leine, R.I., Glocker, C.: Dynamics of a rolling disk in the presence of dry friction. Journal of Nonlinear Science **15**(1), 27–61 (2005)

[92] Collins, B., Hogan, S.: An experimental and theoretical study of euler's disk: Material parameter dependence and motion after falling flat. SIAM Journal on Applied Dynamical Systems **25**(3), 1620–1651 (2026)

[93] Ma, D., Liu, C., Zhao, Z., Zhang, H.: Rolling friction and energy dissipation in a spinning disc. Proceedings of the Royal Society A: Mathematical, Physical and Engineering Sciences **470**(2169), 20140191 (2014)

[94] Kumar, P., Sarkar, D., Gupta, S.C.: Rolling resistance of elastic wheels on flat surfaces. Wear **126**(2), 117–129 (1988)